Inorganic Chemistry

pubs.acs.org/IC

Article

Dopant-Free Hole-Transport Materials with Germanium Compounds Bearing Pseudohalide and Chalcogenide Moieties for Perovskite Solar Cells

Tatiana Soto-Montero, Natalie Flores-Díaz, Desiré Molina, Andrea Soto-Navarro, Andrés Lizano-Villalobos, Cristopher Camacho,* Anders Hagfeldt,* and Leslie W. Pineda*

Cite This: *Inorg. Chem.* 2020, 59, 15154−15166

Read Online

ACCESS | Metrics & More | Article Recommendations | Supporting Information

ABSTRACT: Hole-transport materials (HTMs) are key electronic components for the functioning of perovskite solar cells (PSCs) as they extract the photogenerated holes from the perovskite to be transported subsequently to the back electrode while minimizing the loss from electron recombination. Herein, we report the synthesis and characterization of novel germanium-based compounds with [{HC(CMeNAr)$_2$}GeNCS] (**2**), [{HC(CMeNAr)$_2$}Ge(S)NCS] (**3**), and [{HC(CMeNAr)$_2$}Ge(Se)NCS] (**4**) compositions, with Ar = 2,6-*i*Pr$_2$C$_6$H$_3$ and the photovoltaic performance of **3** and **4** that is the same as for HTM in PSC. All compounds displayed excellent thermal properties and an appropriate alignment of energy levels for the perovskite with maximum optical absorption in the near-UV region. As revealed by space-charge limited-current (SCLC) measurements, compounds **3** and **4** have competing hole mobilities of about 1.37×10^{-4} and 4.88×10^{-4} cm^2 V^{-1} s^{-1}, respectively. Upon assessing PSC devices using **3** and **4** with triple-cation perovskite absorber $Cs_{0.05}(MA_{0.17}FA_{0.83})_{0.95}Pb(I_{0.83}Br_{0.17})_3$, the power conversion efficiencies (PCEs) were about 13.03 and 9.23%, respectively, both without doping and additives, and were compared with benchmark HTM spiro-OMeTAD (2,2′,7,7′-tetrakis(*N*,*N*-di-*p*-methoxyphenylamine)-9,9′-spirobifluorene). Quantum chemical calculations with DFT showed that the optoelectronic properties are strongly influenced by the combined contributions of the germanium atom, the pseudohalide moiety (NCS^-), and chalcogenides (S^{2-} or Se^{2-}). Fine tuning the electronic properties of germanium is thus a good strategy for the targeted synthesis of potential conducting molecules in PSCs.

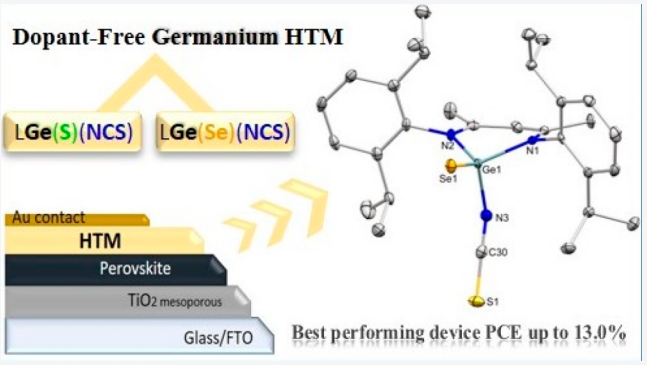

INTRODUCTION

Perovskite solar cells (PSCs) are attracting a large amount of attention due to their astonishing improvement in emerging photovoltaic technologies. Since their first report in 2009,[1] PSC have attained exceptional improvements in performance, achieving certified power conversion efficiencies (PCEs) of up to 25.2% in 2020,[2] overtaking multicrystalline silicon solar cells (23.3%). This rapid evolution of device efficiencies was due mainly to the development of novel deposition techniques and perovskite compositions.[3] Organometal halide perovskites have attractive optoelectronic features: large absorption coefficients,[1] small exciton binding energies (<10 meV),[4] large charge-carrier diffusion lengths,[5] and tunable band gaps.[6] For this reason, much research effort has been devoted to the design and optimization of perovskite materials, the deposition techniques for high-quality perovskite films (e.g., low-temperature solution-processable approaches), and device architectures.[7−14]

As part of the principle of operation of PSC devices, two selective charge-extraction layers are essential to transporting the photogenerated charges (electrons and holes) to the electrodes.[15] In the case of the photogenerated holes, their extraction and transport toward the back electrode are accomplished with components known as hole-transport materials (HTMs) that aim to minimize the electron recombination by preventing direct contact between the perovskite and the back-contact electrode.[16]

At present, the extensive assortments of doped and dopant-free HTMs for perovskite solar devices rely mainly on organic and polymeric backbones, originating from diverse molecular designs. Examples of these scaffolds are 2,2′,7,7′-tetrakis(*N*,*N*-di-*p*-methoxyphenylamine)-9,9′-spirobifluorene (spiro-OMe-

Received: July 17, 2020
Published: October 5, 2020

https://dx.doi.org/10.1021/acs.inorgchem.0c02120
Inorg. Chem. 2020, 59, 15154−15166

Scheme 1. Synthesis Scheme for Compounds 2−4

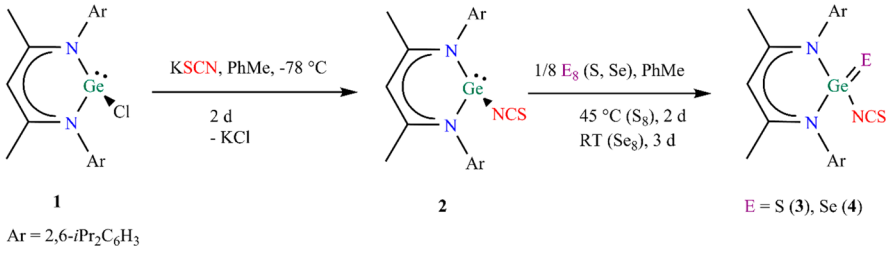

Ar = 2,6-*i*Pr$_2$C$_6$H$_3$

TAD) and polytriarylamines (PTAAs), both of which have found widespread use as hole-transport layers in PSC despite various disadvantages associated with multistep syntheses, coupled with expensive and scanty metal-catalyzed cross-coupling reactions and extensive product purification and reproducibility.[17] Moreover, because spiro-OMeTAD has poor hole mobility in its pristine condition, dopant molecules are added to enhance the hole mobility and the device performance.[18] Doping molecules such as lithium bis(trifluoromethanesulfonyl)imide (LiTFSI) and 4-*tert*-butylpyridine (*t*BP) are hygroscopic and cause damage to the perovskite layer over time.[19−21] In contrast, few examples of inorganic compounds (e.g., CuI, CuSCN, and NiO) acting as HTM have been reported, in part because of the poor solubility that hampers their deposition using spin-coating methods, even though some compounds exhibit excellent electrical and hole conductivities.[22] Some interesting findings have shown the capability of various compounds to work without dopant as HTM, delivering highly efficient PSC.[17] For instance, using optimized undoped spiro-OMeTAD, processed from a non-halogenated solvent (tetrahydrofuran), resulted in 17% PCE with a device containing planar *n*−*i*−*p* architecture.[23] Appending redox-active triphenyl amine (TPA) fragments to a spiro-based HTM followed by annealing afforded, in an inverted (*p*−*i*−*n*) device without dopant, 20.6% PCE and an intrinsic hole mobility of 1 × 10^{-3} cm^2 V^{-1} s^{-1}.[24] Also, organometal-based phthalocyanine and porphyrin molecules, which are structurally related macrocycles, have proven effective as HTM with no dopant. The use of zinc(II) phthalocyanine conjugated dimers with 2,5-thienyl-,2,7-fluorenyl-,3,6-bisthienyldiketopyrrolopyrrole and 1,4-phenyl bridges yielded the best efficiencies, about 15.5−16.8%.[25] The use of Zn(II) porphyrin-based molecules with either push−push (a 5,15-diethynylporphirin core and two lateral *N*,*N*-dialkylaniline groups) or push−pull (*N*,*N*-dialkylaniline and methyl 4-benzoate) traits delivered a PCE of up to 13.10%.[26] Regardless of the chemical categorization, all previous substances function as a hole-conductive layer if they align the energy levels regarding the perovskite, yielding a driving force for the hole injection necessary for hole mobility and conductivity in such devices. Additionally, chemical and physical requirements such as solubility in common organic solvents, synthetically attainable protocols, and thermal stability are pursued.[27]

Our interest in Ge-based molecules stems from the intriguing electronic structure regarding the dual germanium valency (Ge^{2+}, Ge^{4+}), which is associated with charge transport in a semiconducting material.[28] In this context, the incorporation of strong and moderately strong donating ligands, such as isothiocyanate (pseudohalide) and chalcogenides, could result in donor−acceptor Ge-based systems with large hole mobility to transport the holes to the counter electrode. We employed *β*-diketiminate ligands because they resemble the molecular scaffold of porphyrins, which are regarded as light-harvesting units and charge-transport materials in photovoltaics.[29−32] Furthermore, such bidentate ligands are versatile, achieving diverse compounds exhibiting low oxidation states and low coordination geometries because of their steric hindrance and electronic-density donation features, and likewise act as spectator ligands.[33−38]

In this work, we report the synthesis and characterization of germanium compounds with chemical compositions of [{HC(CMeNAr)$_2$}GeNCS] (**2**), [{HC(CMeNAr)$_2$}Ge(S)NCS] (**3**), and [{HC(CMeNAr)$_2$}Ge(Se)NCS] (**4**), where Ar = 2,6-*i*Pr$_2$C$_6$H$_3$, and the evaluation of complete PSC devices based on **3** and **4** as HTM. Compounds **2**−**4** were prepared according to metathesis and oxidative paths, resulting in straightforward synthesis procedures and simple product purification, as indicated by our assessment of the *E* factor.[39,40] To our knowledge, **3** and **4** are the first Ge-based compounds evaluated as organometallic HTM in PSC, specifically having a triple-cation perovskite composition of $Cs_{0.05}(MA_{0.17}FA_{0.83})_{0.95}Pb(I_{0.83}Br_{0.17})_3$.

RESULTS AND DISCUSSION

Synthesis. The metathesis reaction of precursor [{HC(CMeNAr)$_2$}GeCl][41] (**1**) in the presence of KSCN in toluene at −78 °C affords compound [{HC(CMeNAr)$_2$}GeNCS] (**2**) as a yellow solid in 83% yield. The oxidative addition reaction of **2** in toluene with elemental sulfur or red selenium leads to [{HC(CMeNAr)$_2$}Ge(S)NCS] (**3**) and [{HC(CMeNAr)$_2$}Ge(Se)NCS] (**4**) as pale-yellow (65% yield) and lemon-green (77%) solids, respectively (Scheme 1). Compounds **2**−**4** solubilize well in solvents commonly used for HTM in the assembly of PSC such as toluene and chlorobenzene.

The ^{1}H NMR spectrum of **2** exhibits a singlet resonance for the *γ*-C*H* proton of the ligand at *δ* = 5.02 ppm, which, by comparison with that of **1** (*δ* = 5.14 ppm), shows an upfield shift,[41] highlighting the electronic feature of an inductive effect of a pseudohalide moiety smaller than for a halide group; those of **3** and **4** resonate at *δ* = 4.80 and 4.82 ppm, respectively. The latter proton resonances are clearly both shifted to high field, relative to **1** and **2**, which is consistent with an increased electronic density associated with the donor properties from both tethered substituents (pseudohalide and chalcogenide) and a change in the oxidation state of the germanium atom (Quantum Chemical Calculations). The ^{77}Se NMR spectrum of **4** revealed a resonance signal at *δ* = −404.3 ppm, which is in agreement with compounds exhibiting multiple-bond and ylide-type character at the germanium−selenium bond as in [{HC(CMeNAr)$_2$}Ge(Se)OH] (*δ* = −439 ppm; Ar = 2,6-*i*Pr$_2$C$_6$H$_3$),[36] [{HC(CMeNAr)$_2$}Ge(Se)F] (*δ* = −465 ppm),[42] [{HC(CMeNAr)$_2$}Ge(Se)X] (*δ* = −349 and −297 ppm; X = Me, *n*Bu),[42] and [{HC(CMeNAr)$_2$}Ge(Se)Cl] (*δ* = −287

https://dx.doi.org/10.1021/acs.inorgchem.0c02120
Inorg. Chem. 2020, 59, 15154−15166

ppm).[42] The IR spectrum of **2** shows a line at 2041 cm^{-1} ascribed to the stretching vibrational mode of the NCS^- moiety, which is slightly shifted when elemental S_8, as in **3** (2052 cm^{-1}), or Se_8, as in **4** (2025 cm^{-1}), is incorporated (SI Table S1). Regarding the UV−visible absorption spectra of **1**−**4** in chlorobenzene solution, all show absorption bands in the near-UV region, below 370 nm (SI Table S1 and Figure S1), implying no competition for light absorption concerning the perovskite absorber in the visible region.

As β-diketiminate ligands can be prepared without complicated protocols and with readily available chemical reagents, cost-analysis estimates[40,43] for compounds **1**−**4** based on laboratory-scale synthesis were undertaken (SI Schemes S1−S5 and Tables S2−S6). Importantly, the *E* factor, defined as kilograms of waste per kilograms of product,[39] ranges from 72 to 170 for compounds **1**−**4** (detailed calculations in the SI), in sharp contrast to 3600 for spiro-OMeTAD;[40] our processes are hence more efficient in terms of waste materials.

Crystal Structure Analysis. Pale-green single crystals of **4** suitable for X-ray structural analysis were grown from a saturated solution in toluene and pentane kept at ambient temperature for 3 days. Compound **4** crystallizes in monoclinic space group $P2_1/c$ with one molecule in the asymmetric unit. Crystal data, data collection, and details of the structure refinement are summarized in the SI (Tables S7−S10). The molecular structure of **4** consists of a central germanium atom tetrahedrally coordinated with two nitrogen atoms from the monoanionic β-diketiminate ligand, a nitrogen atom from the isothiocyanate group, and a selenium atom (Figure 1).

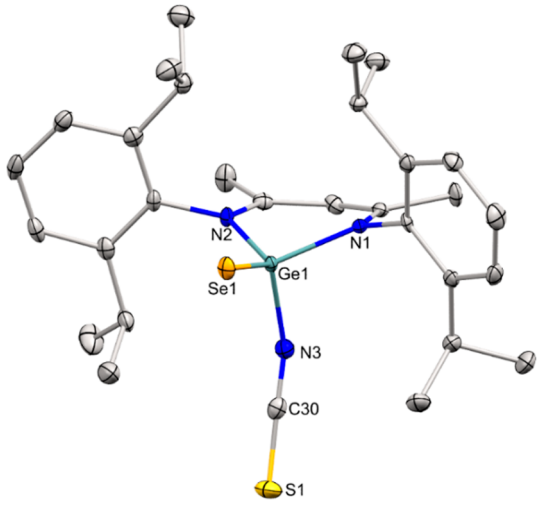

Figure 1. Molecular structure of compound **4**. All hydrogen atoms are omitted for clarity, and thermal ellipsoids are drawn at the 50% probability level.

The length, 2.174(4) Å, of the Ge−Se bond is comparable to those in [{HC(CMeNAr)$_2$}Ge(Se)OH] (2.206(1) Å),[36] [{HC(CMeNAr)$_2$}Ge(Se)Cl] (2.197(6) Å), and [{HC(CMeNAr)$_2$}Ge(Se)(*n*Bu)] (2.219(6) Å),[42] indicating again a resonance-structure contribution from a Ge−Se ylide-type bond and multiple bond character rather than a singly bonded germanium−selenium, of which the bond distances extend from 2.24 to 2.77 Å. With respect to the length (1.901(3) Å) of the Ge−NCS bond in **4**, it is shorter than that in [(*i*Bu)$_2$ATI]GeNCS (2.050(2) Å; ATI = aminotroponiminate), in which the germanium atom is in oxidation state +2.[44]

As for **3**, all attempts to isolate a monocrystalline material suitable for X-ray structure analysis have so far proven unsuccessful.

Thermal, Optoelectronic, and Electrochemical Properties. Thermogravimetric analysis (TGA) of compounds **1**−**4** revealed their excellent thermal stabilities up to 220 °C (Figure 2) and decomposition temperatures (T_{dec}) in the range of

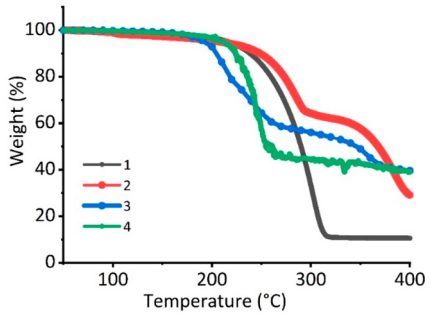

Figure 2. Thermogravimetric curves of compounds **1**−**4**.

Table 1. Thermal Properties of Compounds 1−4 from TGA and DSC

compound	T_{dec}/°C[a]	T_m/°C[b]	T_g/°C[c]
1	293	180	172
2	271	221	215
3	220	212	164
4	240	230	158

[a]Decomposition temperature from TGA. [b]Melting temperature. [c]Glass-transition temperature from DSC.

220−293 °C (Table 1), demonstrating the robustness of these compounds attributed to the chelate effect involving the bidentate β-diketiminate ligand.[45,33,37,38] All of our compounds are thus far above the risk of degradation under typical photovoltaic operating temperatures of between 70 and 90 °C.[46]

The presence of temperatures at which phase transitions of compounds **1**−**4** occur was tested with a differential scanning calorimeter (DSC) (SI Figure S2); detailed thermal features are collated in Table 1. Notably, all thermal transitions in **1**−**4** exceed common operating temperatures of photovoltaic devices[46] and have a range of glass-transition temperatures (T_g) surpassing that of spiro-OMeTAD (125 °C).[47] Having a high T_g affords stable amorphous phases; a decreased tendency to crystallize could prevent device failure over time.[48] Such unwanted trouble is a major concern for spiro-OMeTAD as it tends to crystallize under operating conditions in PSC devices, particularly at elevated temperatures.[49]

We experimentally estimated the optical band gap (E_g) of compounds **1**−**4** from the solid-state UV−visible diffuse reflectance spectra (Figure 3a). On the basis of a modified Tauc plot method[50] (SI Figure S3 and Table S11), the corresponding E_g values denoting directly allowed transitions were calculated to be 2.94, 2.77, 2.84, and 2.86 eV for **1**−**4**, respectively.

The highest-occupied molecular orbital (HOMO) of compounds **1**−**4** was assessed with an experimental determination in solution from cyclic voltammetry (CV) (Figure 3b).

https://dx.doi.org/10.1021/acs.inorgchem.0c02120
Inorg. Chem. 2020, 59, 15154−15166

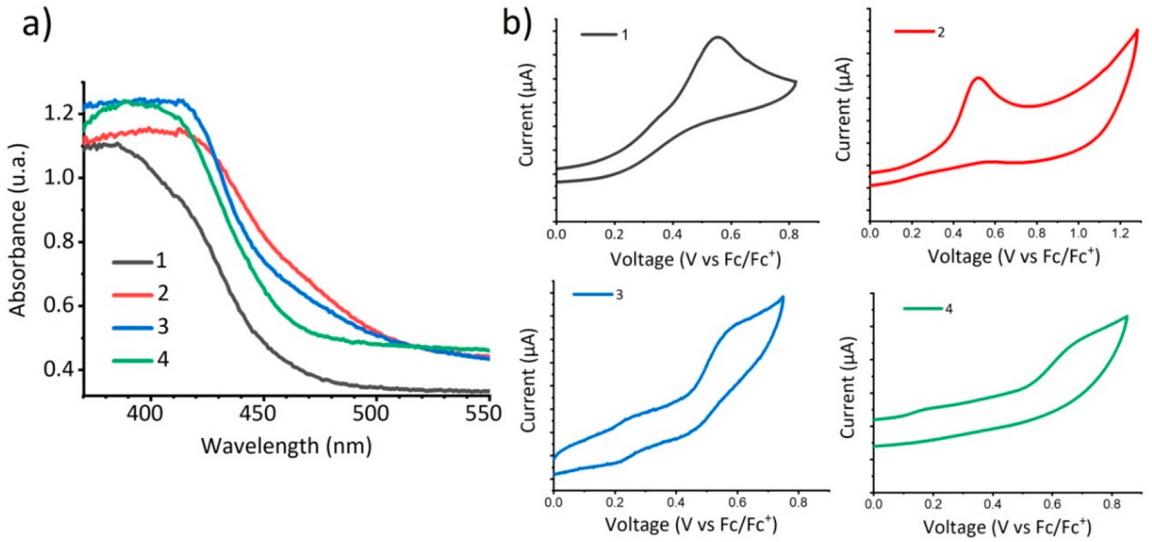

Figure 3. (a) UV−visible absorption spectra of compounds **1**−**4** in the solid state. (b) Cyclic voltammogram of compounds **1**−**4**. Electrolyte: 80:20 LiTFSI (1.0 M) in acetonitrile/chlorobenzene. Scan rate: 100 mV/s.

The resulting HOMO energies are −5.13, −5.18, −5.16, and −5.23 eV for **1**−**4**, respectively. For spiro-OMeTAD under the same experimental conditions, E_{HOMO} is −5.03 eV.

The energy levels of compounds **1**−**4** (Figure 4) were estimated from experimental HOMO from CV and the lowest

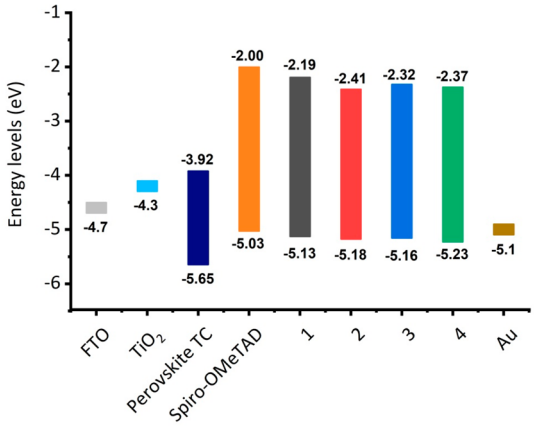

Figure 4. Energy diagram of compounds **1**−**4** and spiro-OMeTAD according to the experimental data. Valence-band (VB) and conduction-band (CB) data for triple-cation perovskite (perovskite TC) from the literature.[52]

unoccupied molecular orbital (LUMO) experimental values (Table 2 and SI Table S12). All HOMO energies evaluated for compounds **1**−**4** are well positioned compared to the triple-cation perovskite valence band (−5.65 eV). Hole injection from the perovskite to the hole carrier is expected to be efficient because of satisfactory energy alignment. Calculated LUMO levels are −2.19 eV for **1**, −2.41 eV for **2**, −2.32 eV for **3**, and −2.37 eV for **4**, which all lie above the perovskite conduction band, −3.92 eV, which indicates their suitable electron-blocking features.

Quantum Chemical Calculations. To acquire insight into the structural and electronic properties of compounds **1**−**4**, we undertook calculations with density functional theory (DFT) at the BP86/def2-TZVP and TD-BP86/def2-TZVP levels of theory for ground and electronically excited states,

Table 2. HOMO, Optical Band Gap (E_g), and LUMO of Compounds 1−4 from the Experimental Methods

compound	HOMO/V vs SHE[a]	HOMO/eV[b]	E_g/eV[c]	LUMO/eV[d]
1	0.732	−5.13	2.94	−2.19
2	0.784	−5.18	2.77	−2.41
3	0.762	−5.16	2.84	−2.32
4	0.832	−5.23	2.86	−2.37
spiro-OMeTAD[e]	0.626	−5.03	−3.03	−2.00

[a]Values from the onset of the first oxidation potential from CV measurements. SHE scale: $HOMO_{vs\ Fc/Fc^+}$ + 0.624.[51] [b]Vacuum scale: −(4.4 + $HOMO_{vs\ SHE}$). [c]Values from a Tauc plot for directly allowed transitions ($(F(R)h\nu)^2$)/eV) according to the UV−visible spectra of compounds in the solid state. [d]([b]HOMO + [c]E_g). [e]Spiro-OMeTAD: HOMO value from CV experimental measurements; E_g from the literature.[22]

respectively. (See the Cartesian coordinates of ground-state optimized geometry in the SI Tables S13−S16). Frontier molecular orbitals and calculated absorption spectra of compounds **1** and **2** (SI Figure S4) and compounds **3** and **4** are shown in Figure 5. Compound **1** shows the main absorption at 344 nm, corresponding to excitation from p orbitals of the chlorine atom to π antibonding orbitals in the central ring. Similarly, compound **2** presents three main excitations at 352, 351, and 342 nm, corresponding to excitations from π antibonding orbitals in the NCS group to π antibonding orbitals in the central ring.

For compound **3**, two main excitations at 324 and 323 nm correspond to electronic transitions from p orbitals of the S atom connected to the Ge atom toward the π antibonding orbitals in the main ring. Following the same pattern as **3**, compound **4** has a main absorption at 325 nm ascribed to excitations from π antibonding orbitals from the NCS group and p orbitals from Se to the central ring.

Natural bond order (NBO) analysis of compounds **1**−**4** shows the germanium atom having charges of 0.99, 1.13, 1.63, and 1.52, respectively. The charge deficiency on the germanium atom for compounds **3** and **4** originates from the electronegativity of its neighboring atoms, as a sulfur atom possesses a greater capability to extract electron density from

https://dx.doi.org/10.1021/acs.inorgchem.0c02120
Inorg. Chem. 2020, 59, 15154−15166

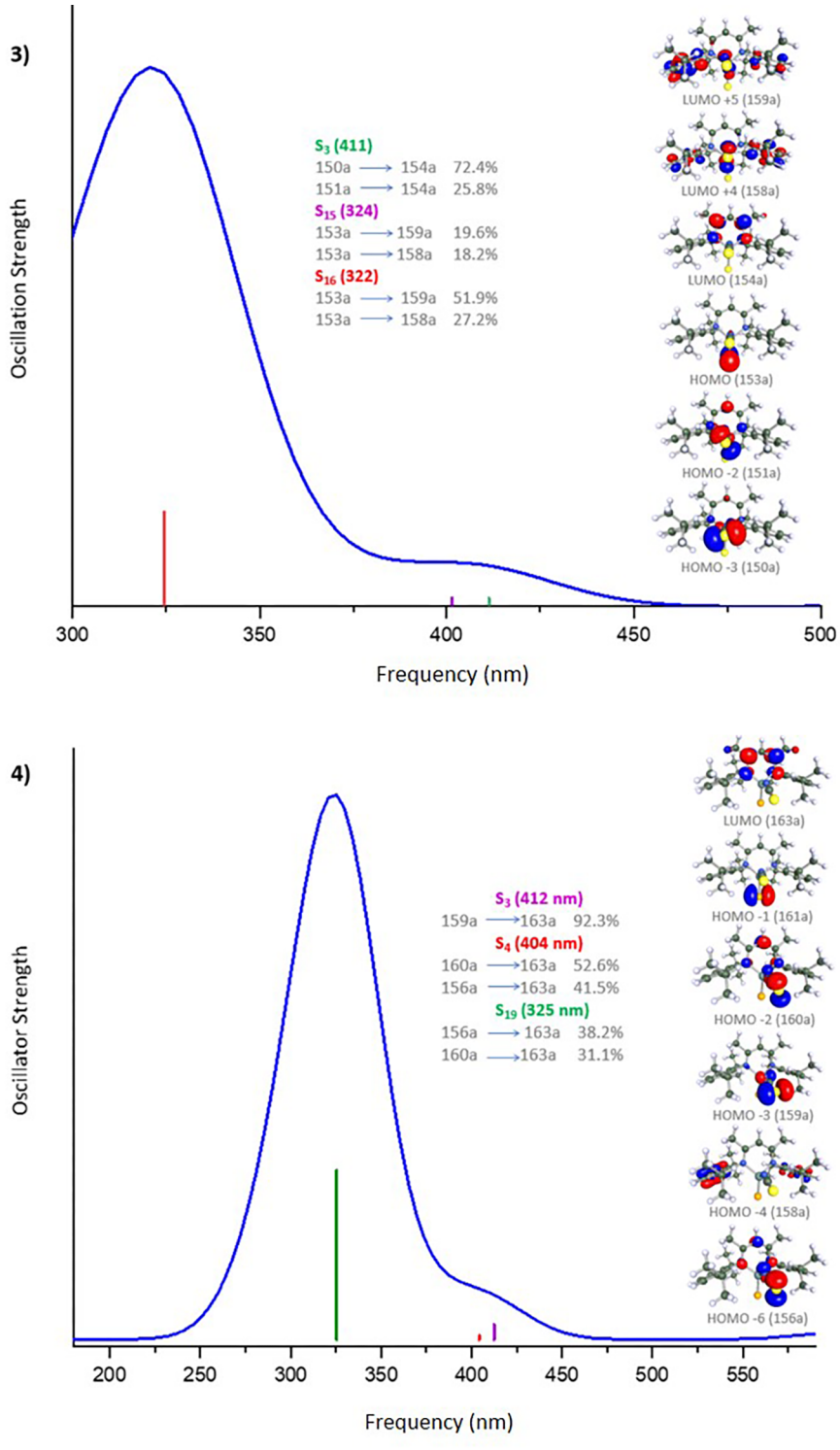

Figure 5. Simulated absorption spectra and frontier molecular orbitals of compounds **3** and **4** computed at the TD-BP86/def2-TZVP and BP86/def2-TZVP levels.

the germanium atom than from the selenium atom. As observed from the frontier molecular orbitals of **3** and **4** and the corresponding electronic transitions generating the features appearing in the window of interest in terms of wavelength in the simulated UV−visible spectra (Figure 5), the germanium atom acts as a bridge to move charge from the isothiocyanate group to the central ring. The charge deficiency of the bridge-like Ge atom is enhanced by the attachment of the chalcogenides by oxidative addition, altering the oxidation state from Ge(II) to Ge(IV) as in **3** and **4**.

Periodic calculations of compounds **1**−**4** show two distinct spatial arrangements among them. Compound **1** shows stacking on the central ring, containing the germanium atom, creating a layered structure in which the chlorine atoms align antiparallel, which allows for stabilization by minimizing their repulsion. In addition to those mentioned above, the

https://dx.doi.org/10.1021/acs.inorgchem.0c02120
Inorg. Chem. 2020, 59, 15154−15166

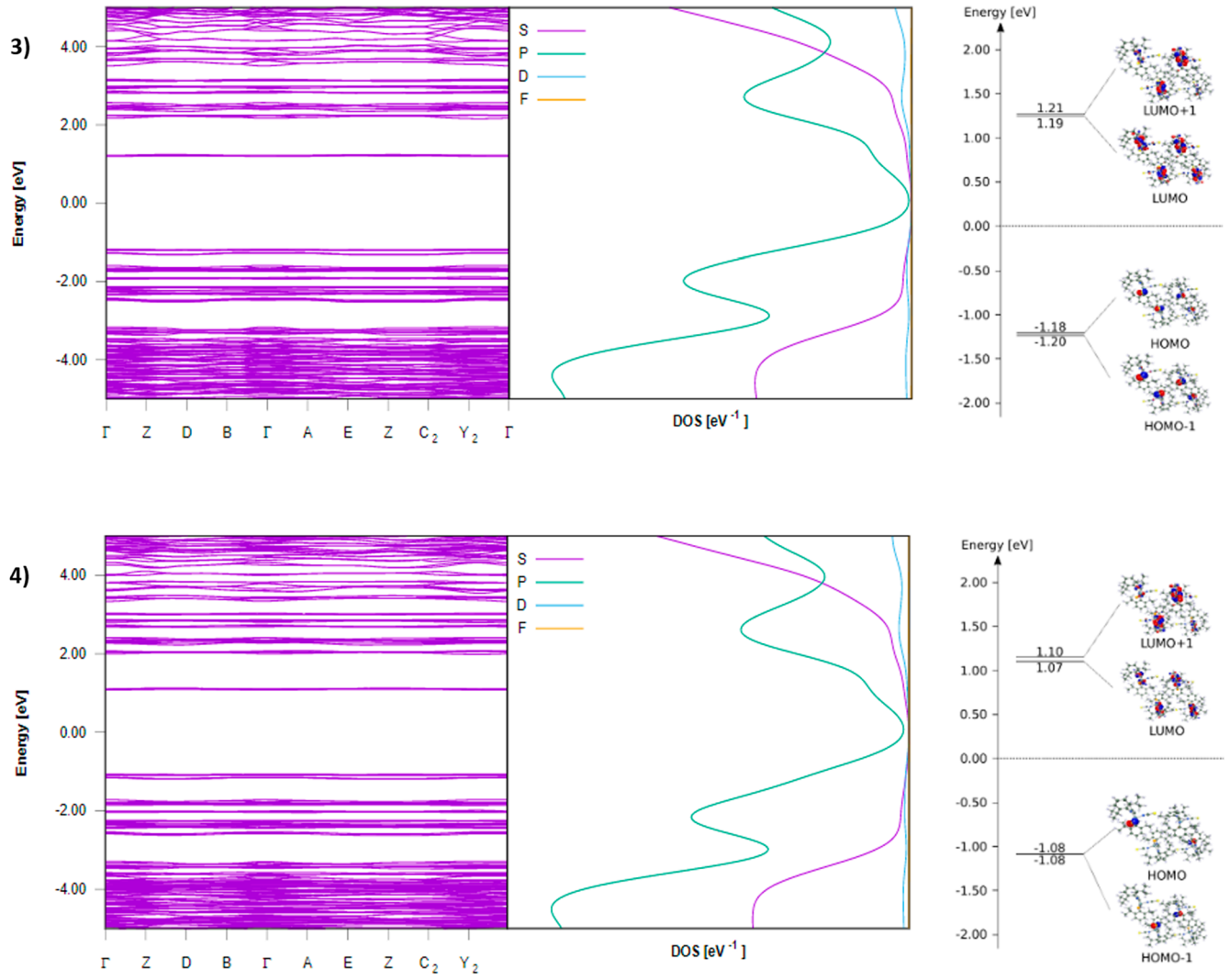

Figure 6. Band structure, DOS, and unit-cell frontier molecular orbitals of compounds **3** and **4**.

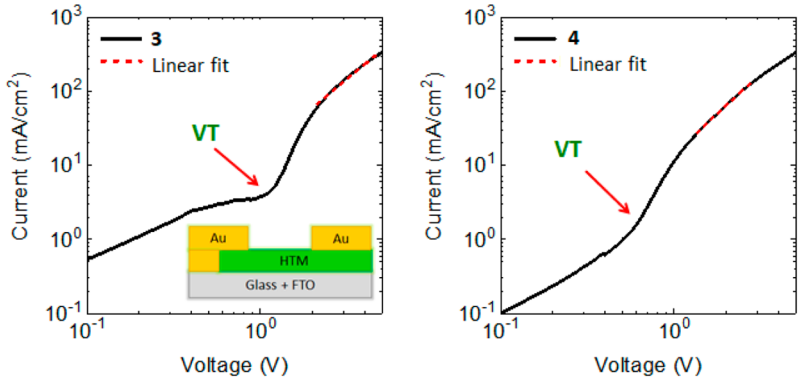

Figure 7. Current density−voltage curves from space−charge-limited current measurements of compounds **3** and **4** on hole-only devices. Inset: device architecture.

substituents on the benzene rings move apart from the Cl atoms, producing an out-of-plane arrangement of the Ge atoms with respect to the central ring. In contrast, **2**−**4** display a distorted bicolumnar arrangement of the central rings with the NCS substituent aligning in an antiparallel configuration with rotation 90° with respect to the stacking axis. Optimized cell parameters are given in SI Table S17, according to which the inclusion of S and Se atoms evidently increases the packing of their unit cells, allowing for enhanced intramolecular interactions.

Theoretically computed band gaps provided in SI Table S18 reveal a trend in which the gap decreases with the increment in the number of electrons per unit cell. The density of states (DOS) plots and their corresponding atomic contributions (SI

https://dx.doi.org/10.1021/acs.inorgchem.0c02120
Inorg. Chem. 2020, 59, 15154−15166

Figure S5 and Figure 6) show that all bands near the Fermi level have a majority p character for the four systems studied. From the frontier molecular orbital analysis of the unit cells of **1**−**4**, p orbitals evidently constitute valence bands from the substituents bonded to the Ge atom. Moreover, as a second substituent is attached to the Ge atom, the orbitals tend to be localized on the second substituent, namely, S and Se.

Plots of the density of states and molecular orbitals make clear that conduction bands are always localized in the central ring for **1**−**4**, with π antibonding character. An analysis of the electronic charge shows that increasing the electronegativity of the atom attached to the Ge atom decreases its electron density, which facilitates the charge mobility from the valence band to the π system in the central ring. The latter computed results imply that compounds **3** and **4** bestow effective electronic properties for hole extraction due to the contribution of the central atom, with pseudohalide and chalcogenide donating ligands in comparison with compounds **1** and **2**. In practice, the latter two compounds give a short-circuit response upon measuring the hole mobility experimentally (no data were collected). Likewise, the PCE in complete perovskite devices was less than 1%.

Charge-Transport Properties: Hole Mobility. The electrical properties of compounds **3** and **4** were measured with space−charge-limited current (SCLC) in a hole-only device with configuration FTO/HTM/Au.[53] Figure 7 depicts typical *J*−*V* curves of SCLC in which ohmic and space−charge regions are divided by the specific voltage (*VT*). The inset shows the sandwich-type architecture containing only hole-transport compounds; hole mobility values obtained are shown in Table 3.

Table 3. Hole Mobility of Compounds 3 and 4

HTM	hole mobility/cm^2 V^{-1} s^{-1}
3	1.37×10^{-4}
4	4.88×10^{-4}
spiro-OMeTAD (pristine)[a]	2.69×10^{-5}
spiro-OMeTAD + LiTFSI + *t*BP[a]	3.78×10^{-3}

[a]Data from the literature.[19]

Notably, the hole mobility was 1.37×10^{-4} cm^2 V^{-1} s^{-1} for **3** and 4.88×10^{-4} cm^2 V^{-1} s^{-1} for **4**, both about 10 times that of pristine spiro-OMeTAD (2.69×10^{-5} cm^2 V^{-1} s^{-1}) and various hole-transport materials with high efficiencies in PSC.[22] Our preliminary results for compounds **3** and **4** are noteworthy for having charge transport without dopant addition as both surpass pristine spiro-OMeTAD, whereas doping with LiTFSI or *t*BP yielded no further improvement.

Again, for compounds **1** and **2** ohmic contact issues and short circuits were observed in hole-only devices; further experimental analysis would be necessary to assess such behavior.[54]

Photovoltaic Characterization. The performance of **3** and **4** as HTM was evaluated with a triple-cation perovskite employing a regular mesoporous architecture, FTO/cp-TiO_2/mp-TiO_2/perovskite/Ge-HTM/Au, measured under solar simulator AM 1.5 G conditions with 100 mW cm^{-2} light intensity and with a 0.16 cm^2 mask of active area. To achieve excellent film-forming properties and efficient photovoltaic performance with the germanium compounds, optimizations were undertaken in terms of solvents and concentrations (further details in SI Figure S6). According to these tests, solutions of compounds **3** (45 mM) and **4** (15 mM) in chlorobenzene were used for spin-coating depositions.

The film thickness of compounds **3** and **4** was accessed with images from a high-resolution cross-sectional scanning electron microscope (SEM) of the complete devices, glass/FTO/-TiO_2/perovskite/Ge-compound/Au (Figure 8). These cross-sectional images reveal a uniform film thickness and excellent coverage of the deposited layers of **3** and **4**, similar to those of spiro-OMeTAD.[55] The films of compounds **3** and **4** yield thin layers of approximately 200 nm sandwiched between the perovskite and the gold contact layer, with the perovskite films showing crystals of appropriate size and homogeneity.

As *J*−*V* curves in Figure 9 and Table 4 show, compound **3** shows the best performance with a PCE of 13.03%, a photocurrent density of 22.1 mA cm^{-2}, a photovoltage of 0.94 V, and a fill factor of about 0.64. The best device for compound **4** had a PCE of 9.23%, a photocurrent density of 18.2 mA cm^{-2}, a photovoltage of 0.91 V, and a fill factor of 0.56. All *J*−*V* curves presented in Figure 9 correspond to a reverse scan. Preliminary measurements of forward and reverse scans for compound **3** (SI Figure S7 and Table S19) show that the best results were obtained with measurements in reverse scan mode; further study is required to understand the origins of this effect and to improve the hysteresis.

Photovoltaic parameters of multiple devices are presented as box plots in SI Figure S8.

Compound **3** exceeds the efficiency of undoped spiro-OMeTAD, whereas **4** achieves comparable efficiency (Table 4). The fill factors obtained with compounds **3** and **4** are superior to that of pristine spiro-OMeTAD, which improved only upon doping. Our compounds instead show that upon doping the performance diminished, proving that they work better as dopant-free HTM. Such findings are ascribed to some extent to the hole mobility attained for compounds **3** and **4**, which is ∼10 times that reported for pristine spiro-OMeTAD.[19]

Nevertheless, complete devices for both novel compounds did not surpass the pristine spiro-OMeTAD photocurrent density. For compound **3**, the overall large efficiency of the incident photon to current (IPCE) is between 80 and 60% for the entire visible wavelength range; that of compound **4** is about 80% over the entire range (SI Figure S9). In these IPCE plots, the difference between **3** and **4** is seen mainly at wavelength greater than 550 nm; such behavior can be tentatively associated with interfacial processes between the perovskite and germanium-HTM, which in turn affect the efficiency of charge collection, mainly when charge recombination occurs during charge-carrier transport. The suppression of the recombination by appropriate interfacial engineering is therefore important.[56] In this context, we also do not rule out that the presence of sulfur in **3** might have a beneficial effect on PSC performance; sulfur-doped all-inorganic perovskite materials have demonstrated superior stability with efficient devices relative to control devices without the aid of doping.[57] Halide perovskite devices with sulfur treatments of interfacial layers resulted in the passivation of the charge traps, the mitigation of interfacial recombination, and changes in the charge-transport kinetics at the interface.[58] These results indicate that there is scope for improving the complete devices of compounds **3** and **4** with further optimization of their interfacial engineering and the processes involved (e.g., experiments on photoexcited charge-carrier recombination dynamics).

https://dx.doi.org/10.1021/acs.inorgchem.0c02120
Inorg. Chem. 2020, 59, 15154−15166

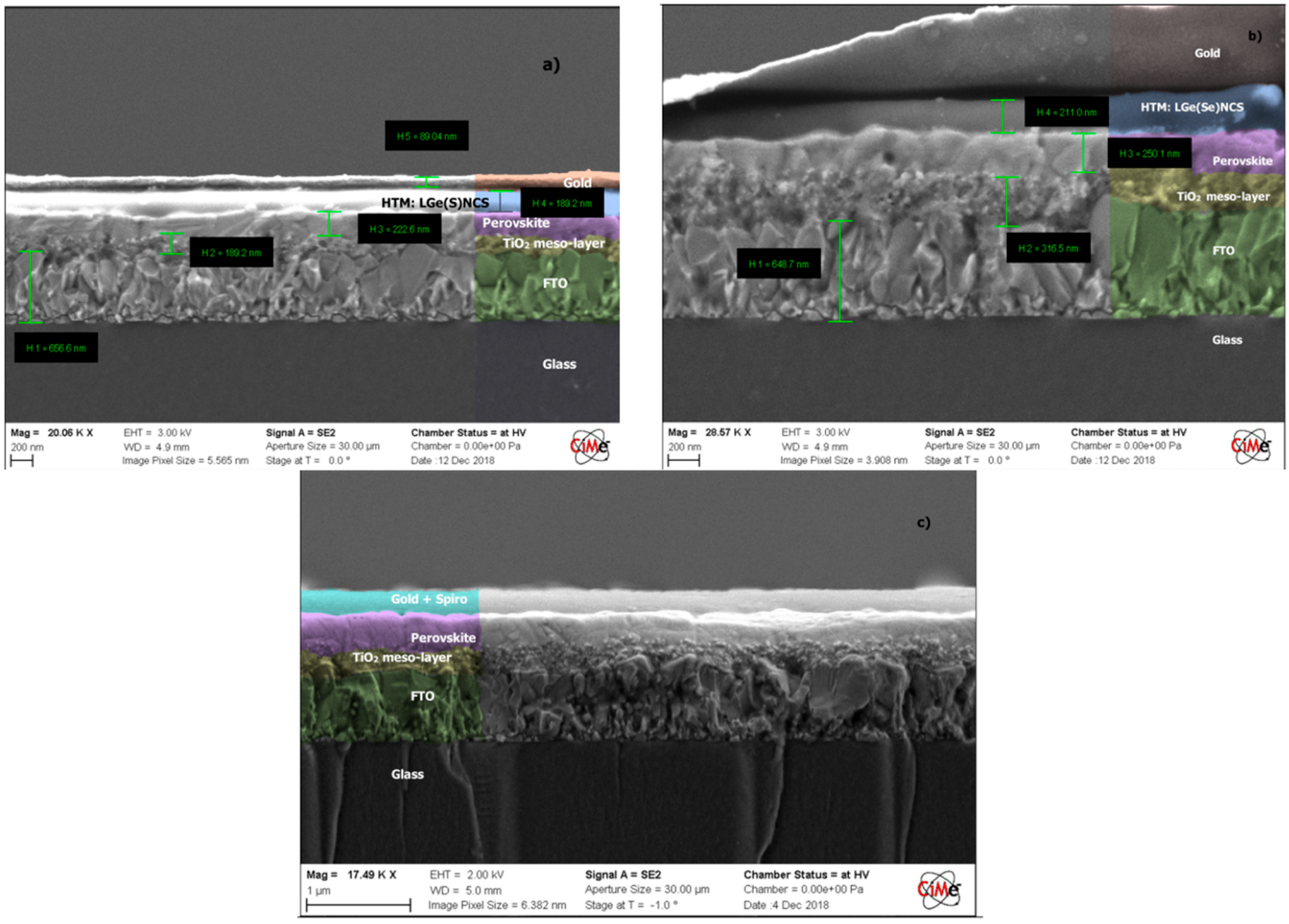

Figure 8. Cross-sectional scanning electron microscope (SEM) images of regular architecture triple-cation perovskite solar cells with (a) compound **3**, (b) compound **4**, and (c) spiro-OMeTAD as HTM.

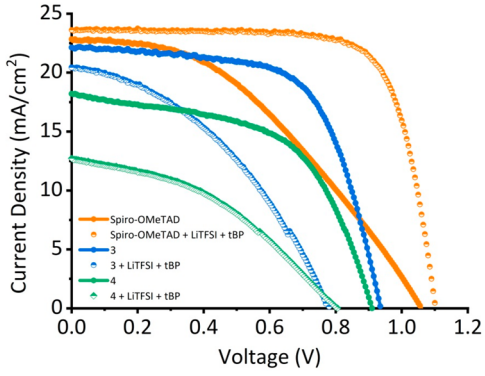

Figure 9. Current−voltage (J−V) curves of the best-performing devices of compounds **3** and **4** and spiro-OMeTAD as HTM, pristine, and doped with LiTFSI and *t*BP. Devices employing triple-cation perovskite $[Cs_{0.05}(MA_{0.17}FA_{0.83})_{0.95}Pb(I_{0.83}Br_{0.17})_3]$, with reverse scans.

Table 4. Photovoltaic Parameters of the Best-Performing Complete Devices Employing Compounds 3 and 4 and spiro-OMeTAD, Pristine as Well as Doped with LiTFSI and *t*BP

compound	J_{SC} (mA cm^{-2})	V_{OC} (V)	FF	PCE (%)
3	22.1	0.94	0.64	13.03
4	18.2	0.91	0.56	9.23
3 + LiTFSI + *t*BP	20.4	0.78	0.40	6.36
4 + LiTFSI + *t*BP	12.7	0.81	0.40	4.04
spiro-OMeTAD	22.8	1.06	0.41	9.81
spiro-OMeTAD + LiTFSI + *t*BP	23.6	1.10	0.74	19.29

CONCLUSIONS

We report the first synthesis of organogermanium compounds bearing strong or moderately strong σ-donating ligands such as pseudohalides (isothiocyanate) and chalcogenides (S and Se).

Our innovative approach takes advantage of the dual germanium valency to tune the donor−acceptor properties as demonstrated by computational, optical, and electrochemical means, rendering excellent band alignments for application as HTM. The latter electronic synergy enables enhanced hole mobility of compounds **3** and **4**, about 10 times that of the undoped spiro-based counterpart. Moreover, these germanium-based compounds are readily synthesized with the advantage of being solution-processable to form hole-transport layers in perovskite solar cells.

In assessing compounds **3** and **4** as HTM in perovskite solar devices, we found that, without dopants or additive substances, satisfactory efficiency was attained for compounds **3** (13.03%)

https://dx.doi.org/10.1021/acs.inorgchem.0c02120
Inorg. Chem. 2020, 59, 15154−15166

and **4** (9.23%) relative to benchmark compound pristine spiro-OMeTAD.

Designing molecules with novel electronic interactions to function as HTM could benefit from the variety of elements in the periodic table, as highlighted by the bridge-like germanium behavior, transporting charge from donating moieties to an electron-deficient central core. This strategy provides opportunities to bond germanium to arylamines, diphenylamines, triarylamines, bis(trifluoromethanesulfonyl)imide and porphyrins, which are all potential HTMs in perovskite devices.

EXPERIMENTAL SECTION

All experimental manipulations were undertaken with standard Schlenk line and glovebox techniques under a dry nitrogen atmosphere. 2,6-Diisopropylaniline (Sigma-Aldrich), 2,4-pentanedione (Sigma-Aldrich), $GeCl_2$·diox (Sigma-Aldrich), *n*BuLi (solution 2.5 M in hexanes, Sigma-Aldrich), KSCN (Sigma-Aldrich), $PbBr_2$ (99.99%, TCI), PbI_2 (99.99%, TCI), formamidinium iodide (FAI, Dyesol), methylammonium bromide (MABr, Dyesol), CsI (99.998, ABCR), RbI (99.9%, Sigma-Aldrich), LiTFSI (99.95%, Sigma-Aldrich), spiro-OMeTAD (Dyesol), *t*BP (Sigma-Aldrich), chlorobenzene (99.8% extra dry, Acros), DMF (99.8% extra dry, Acros), DMSO (99.8% extra dry, Acros), and acetonitrile (99.8% extra dry, Acros) were used as received. Red amorphous selenium (Se_8) was prepared according to the literature procedure.[59] Sulfur (S_8) was recrystallized from toluene before use. Solvents were purified according to conventional procedures and were freshly distilled over appropriate drying agents under a dry nitrogen atmosphere before use; toluene, pentane, and deuterated benzene (C_6D_6) were dried with a sodium benzophenone mixture; tetrahydrofuran and diethyl ether were dried with MBraun Solvent Purification Systems (MS-SPS). The samples for spectral measurements were prepared in a glovebox (Lab MBraun workstation). An NMR spectrometer (Bruker 400 MHz) was used to record ^{1}H and ^{13}C chemical shifts, both reported with reference to the resonances of the solvent used. The ^{77}Se NMR spectrum was acquired at 14.1T (600 MHz for ^{1}H) at 298 K on a Bruker AVIII spectrometer equipped with a 5 mm N_2-cooled cryoprobe summing 256 transients. Residual ^{1}H resonance from deuterated C_6D_6 solvent was used to reference the ^{1}H spectrum with the methyl resonance of TMS at 0.0 ppm. The ^{77}Se chemical shift was referenced using the unified chemical shift scale, according to an IUPAC-recommended method.[60] Compounds [{HC(CMeNAr)$_2$}Li(Et$_2$O)] and [{HC(CMeNAr)$_2$}-GeCl] (**1**) were prepared according to the literature procedures.[61,41]

Preparation of Compound [{HC(CMeNAr)$_2$}GeNCS] (2). To a suspension of KSCN (0.53 g, 5.42 mmol) in toluene (20 mL) at −78 °C was added via cannula a solution of **1** (2.85 g, 5.42 mmol) in toluene (40 mL). A light-yellow solution appeared after 2 h, which remained unchanged after stirring for 2 days. Subsequent filtration and removal of solvent gave a light-yellow solid. Keeping a solution of **2** (0.5 g) dissolved in a minimum amount of toluene and pentane (2 mL) in a freezer (−20 °C) for 7 days gave light-yellow crystals. Yield: 2.47 g, (83%). Mp: 223−225 °C. Elemental anal. calcd for $C_{30}H_{41}N_3GeS$ (548.37 g mol^{-1}): C, 65.71; H, 7.54; N, 7.66. Found: C, 65.90; H, 7.52; N, 7.65. UV−vis (λ_{max}, chlorobenzene) nm {ε/dm^3 mol^{-1} cm^{-1}}: 362 {16 686}. IR (ATR): $\tilde{\nu}$ 2041 cm^{-1} (NCS$^-$). ^{1}H NMR (400 MHz, C_6D_6, Me_4Si): δ 6.98−7.13 (m, 6H, *m*-, *p*-Ar*H*), 5.02 (s, 1H, γ-C*H*), 3.63 (sept, 2H, $^3J_{HH}$ = 6.8 Hz, C*H*(Me)$_2$), 2.95 (sept, 2H, $^3J_{HH}$ = 6.8 Hz, C*H*(Me)$_2$), 1.58 (d, 6H,$^3J_{HH}$ = 6.8 Hz, CH(*Me*)$_2$), 1.48 (s, 6H, *Me*), 1.30 (d, 6H, $^3J_{HH}$ = 6.8 Hz, CH(*Me*)$_2$), 1.14 (d, 6H, $^3J_{HH}$ = 6.8 Hz, CH(*Me*)$_2$), 0.96 (d, 6H, $^3J_{HH}$ = 6.8 Hz, CH(*Me*)$_2$). ^{13}C NMR (100 MHz, C_6D_6, Me_4Si): δ 165.4 (*C*N), 146.6, 143.0, 139.2, 127.9, 125.1, 123.7 (*i*-, *o*-, *m*-, *p*-*Ar*), 101.2 (γ-CH), 29.0 (CH(Me)$_2$), 28.4 (*C*H(Me)$_2$), 26.7 (*Me*), 24.2 (CH(*Me*)$_2$), 24.0 (CH(*Me*)$_2$), 23.6 (CH(*Me*)$_2$), 22.7 (CH(*Me*)$_2$).

Preparation of Compound [{HC(CMeNAr)$_2$}Ge(S)NCS] (3). A solution of **2** (5 g, 9.12 mmol) in toluene (40 mL) was slowly added to a suspension of freshly recrystallized elemental sulfur (0.29 g, 9.12 mmol) in toluene (15 mL) via cannula at ambient temperature. After constant stirring at 45 °C for 3 days, the light-yellow solution turned pale yellow. After the removal of all volatiles, the remaining crude product was rinsed with hexane (3 × 10 mL) and dried under reduced pressured to yield pure **3**. Storage of a solution of **3** (0.5 g), dissolved in a minimum amount of toluene and pentane (2 mL) in a freezer (−20 °C) for 7 days, yielded colorless crystals. Yield: 3.44 g (65%). Mp: 193−195 °C (dec). Elemental anal. calcd for $C_{30}H_{41}N_3GeS_2$ (580.44 g mol^{-1}): C, 62.10; H, 7.12; N, 7.24. Found: C, 62.05; H, 7.15; N, 7.23. UV−vis (λ_{max}, chlorobenzene) nm {ε/dm^3 mol^{-1} cm^{-1}}: 293 {13 391} and 367 {16 882}. IR (ATR): $\tilde{\nu}$ 2052 cm^{-1} (NCS$^-$). ^{1}H NMR (400 MHz, C_6D_6, Me_4Si): δ 7.03−7.12 (m, 6H, *m*-, *p*-Ar*H*), 4.80 (s, 1H, γ-C*H*), 3.40 (sept, 2H, $^3J_{HH}$ = 6.8 Hz, C*H*(Me)$_2$), 3.11 (sept, 2H, $^3J_{HH}$ = 6.8 Hz, C*H*(Me)$_2$), 1.60 (d, 6H, $^3J_{HH}$ = 6.8 Hz, CH(*Me*)$_2$), 1.40 (d, 6H, $^3J_{HH}$ = 6.8 Hz, CH(*Me*)$_2$), 1.36 (s, 6H, *Me*), 1.25 (d, 6H, $^3J_{HH}$ = 6.8 Hz, CH(*Me*)$_2$), 0.95 (d, 6H, $^3J_{HH}$ = 6.8 Hz, CH(*Me*)$_2$). ^{13}C NMR (100 MHz, C_6D_6, Me_4Si): δ 170.8 (*C*N), 146.0, 143.9, 135.8, 129.1, 124.9, 124.3 (*i*-, *o*-, *m*-, *p*-*Ar*), 100.1 (γ-CH), 29.2 (CH(Me)$_2$), 28.8 (*C*H(Me)$_2$), 25.9 (*Me*), 24.1 (CH(*Me*)$_2$), 24.0 (CH(*Me*)$_2$), 23.6 (CH(*Me*)$_2$), 23.4 (CH(*Me*)$_2$).

Preparation of Compound [{HC(CMeNAr)$_2$}Ge(Se)NCS] (4). To a suspension of elemental red selenium (0.29 g, 3.65 mmol) in toluene (20 mL) was added via cannula a solution of **2** (2.0 g, 3.65 mmol) in toluene (40 mL). A lemon-green solution appeared after 30 min, which remained unchanged after stirring for 2 days. Subsequent filtration and removal of solvent gave a dark-yellow solid. **4** (0.5 g) was dissolved in a minimum amount of toluene and pentane (2 mL) and kept at ambient temperature for 3 days to afford lemon-green crystals. Yield: 1.77 g (77%). Mp: 180−182 °C (dec). Elemental anal. calcd for $C_{30}H_{41}N_3GeSeS$ (627.33 g mol^{-1}): C, 57.44; H, 6.59; N, 6.70. Found: C, 57.42; H, 6.56; N, 6.68. UV−vis (λ_{max}, chlorobenzene) nm {ε/dm^3 mol^{-1} cm^{-1}}: 351 {15 918}. IR (ATR): $\tilde{\nu}$ 2025 cm^{-1} (NCS$^-$). ^{1}H NMR (400 MHz, C_6D_6, Me_4Si): δ 7.03−7.13 (m, 6H, *m*-, *p*-Ar*H*), 4.82 (s, 1H, γ-C*H*), 3.40 (sept, 2H, $^3J_{HH}$ = 6.8 Hz, C*H*(Me)$_2$)), 3.08 (sept, 2H, $^3J_{HH}$ = 6.8 Hz, C*H*(Me)$_2$)), 1.62 (d, 6H, $^3J_{HH}$ = 6.8 Hz, CH(*Me*)$_2$)), 1.42 (d, 6H, $^3J_{HH}$ = 6.8 Hz, CH(*Me*)$_2$)), 1.38 (s, 6H, *Me*), 1.25 (d, 6H, $^3J_{HH}$ = 6.8 Hz, CH(*Me*)$_2$)), 0.95 (d, 6H, $^3J_{HH}$ = 6.8 Hz, CH(*Me*)$_2$)). ^{13}C NMR (100 MHz, C_6D_6, Me_4Si): δ 170.4 (*C*N), 146.1, 143.9, 136.0, 129.1, 124.9, 124.3 (*i*-, *o*-, *m*-, *p*-*Ar*), 100.4 (γ-CH), 29.3, (CH(Me)$_2$), 28.9 (*C*H(Me)$_2$), 26.0 (*Me*), 24.1(CH(*Me*)$_2$), 24.0 (CH(*Me*)$_2$), 23.7 (CH(*Me*)$_2$), 23.6 ppm (CH(*Me*)$_2$). ^{77}Se NMR (600 MHz for ^{1}H, C_6D_6, 25 °C): −404.3 ppm.

Preparation of Substrates. A glass substrate (Nippon sheet glass, 10 Ω sq^{-1}) with FTO substrates was cleaned vigorously but without scratching, using a cleaning solution (Hellmanex 10%) diluted with water, and then subjected to cleaning three times in an ultrasonic bath: (1) in an aqueous solution (2% Hellmanex, Hellma GmbH) for 20 min, (2) in an acetone bath for 15 min, and (3) in an ethanol bath for 15 min. After ultrasonication, the substrates were rapidly dried in a strong flow of air. UV-ozone cleaning for 15 min at maximum power was carried out before an application of the TiO_2 compact layer.

Bottom Selective Contacts. FTO substrates were rapidly warmed to 450 °C (within 15 min) and then left for 15 min at 450 °C before deposition of the compact TiO_2 layer with aerosol spray pyrolysis. The sprayed solution was made with a precursor solution of anhydrous ethanol (EtOH, 9 mL), 2,4-pentanedione (400 μL), and titanium diisopropoxide bis(acetylacetonate) (600 μL); the mixture was stirred manually for 1 min and then added with a nozzle. The substrates were kept at 450 °C for 10 min and then slowly cooled to near 23 °C. The mesoporous TiO_2 layer was prepared with TiO_2 paste (30 N-RD Dyesol) diluted in ethanol as 1:6 w/w. The resulting dispersion was stirred vigorously overnight before use. To prepare the mesoporous TiO_2 layer, a dispersion (50 μL) was added dropwise over the TiO_2 compact layer and then spin-coated using acceleration at 4000 and 2000 rpm/s for 20 s. Immediately after the spin coating, the layer was dried at 100 °C for 10 min and subsequently sintered with multiple temperature steps up to 450 °C.

Preparation and Deposition of the Perovskite Precursor Solution. Stock solutions (1.5 M) of PbI_2 and $PbBr_2$ in 4:1

https://dx.doi.org/10.1021/acs.inorgchem.0c02120
Inorg. Chem. 2020, 59, 15154−15166

dimethylformamide (DMF)/dimethyl sulfoxide (DMSO) were prepared by heating the solutions from 23 to 180 °C for 10 min or until the dissolution of the salts was complete (clear solution). A CsI stock solution (1.5 M) in DMSO was prepared on heating to 150 °C until the solid was completely dissolved. Methylammonium bromide (MABr) and formamidinium iodide (FAI) powders were weighed in two separate vials. To determine the amount of solid from MABr and FAI, one must consider the 1:1.09 stoichiometry of FAI/PbI_2 (MABr/$PbBr_2$) (i.e., 9% excess lead) for final solutions (1.22 M) of $FAPbI_3$ and $MAPbBr_3$. Finally, CsI/$FAPbI_3$/$MAPbBr_3$ 0.3:5:1 v/v/v solutions were mixed. The perovskite solution was deposited using the following two-step spin-coating protocol: a static slow step (1000 rpm, 200 rpm/s, 10 s) after adding perovskite solution (50−60 μL) to the middle of the substrate for appropriate surface coverage and a subsequent rapid step (6000 rpm, 2000 rpm/s, 20 s). In the second step, the antisolvent (chlorobenzene, 100 μL) was dropped 5 min before the end of the step onto the middle of the rotating substrate with a pipet. Finally, substrates were placed on a preheated hot plate at 100 °C for 40−60 min. After the annealing, substrates were left to cool to ca. 23 °C (15−20 min).

Deposition of a Hole-Transport Layer. For the hole-transport layers of **3** and **4**, several parameters such as concentrations and solvents (chlorobenzene and toluene) were tested and optimized to achieve the best PV properties. Concentrations of **3** and **4** were varied from 10 to 100 mg/μL; we found that 45 mg/μL (**3**) and 15 mg/ μL (**4**) gave superior PV properties. A solution (60 μL) in chlorobenzene (45 mM for **3** and 15 mM for **4**) was hence added to the middle of the perovskite film with spin coating (4000 rpm, 2000 rpm/s, 20 s) in a one-step protocol.

For the reference cell, spiro-OMeTAD in chlorobenzene served as the hole-transport material. Devices were prepared with and without LiTFSI and *t*BP additives. For the spiro-OMeTAD standard solutions, spiro-OMeTAD powder (45 mg) was dissolved in chlorobenzene (500 μL) and doped with a LiTFSI stock solution (10.31 μL, 52 mg of LiTFSI in 100 μL of MeCN) and *t*BP (17.75 μL). A spiro-OMeTAD doped solution (50 μL) was added to the middle of the perovskite film using spin coating (4000 rpm, 2000 rpm/s, 20 s) in a one-step protocol.

Evaporation of Metal Electrodes. Gold layer contacts (thickness 80 nm) were deposited over the HTM in the device with a mask according to the method of thermal evaporation.

Thermogravimetric Analysis. Thermogravimetric analysis (TGA) was performed (TGA Q 500 instrument). Samples were subjected to a heating cycle from ambient temperature to 300 °C at scanning rate of 10 °C/min under a nitrogen atmosphere. Decomposition temperatures (T_{dec}) were derived from the plots. The glass-transition temperature T_g and melting temperature T_m were obtained with a differential scanning calorimeter (PerkinElmer DSC8000). Samples were subjected to two consecutive heating and cooling cycles from ambient temperature to 220−240 °C at scanning rate of 10 °C/min under a nitrogen atmosphere.

Ultraviolet−Visible Spectral Measurements. Optical properties were measured with a UV−visible spectrophotometer (Evolution 600, Thermo Scientific). UV−visible absorption spectra were recorded on samples in a solution of chlorobenzene at a concentration of 1.0×10^{-5} M with a quartz cuvette (optical path 1 cm). Spectra were recorded in the wavelength range of 300−800 nm. UV−visible diffuse reflectance spectra were also recorded with a UV−visible spectrophotometer (Evolution 600) and an integrating sphere (DRA-EV-600, constructed of Spectralon, standard). Labsphere's highest reflectance material served to calibrate the equipment. The optical absorption was measured in the range of 250−850 nm. Reflectance values were converted to a magnitude of $F(R)$ and plotted versus energy according to the Kubelka−Munk method: $F(R) = (1 - R)^2/2R$, where R corresponds to the reflectance values. To estimate values of optical band gaps (E_g), we applied the Tauc plot method as $(F(R)h\nu)^n$, where h is the Planck constant (J·s) and ν is the frequency (s^{-1}) of light; the value of n depends on the specific transition coefficient: we used $n = 1/2$ for a directly allowed transition (plotted as $\alpha(h\nu)^2$ versus E).

Cyclic Voltammetry (CV). Cyclic voltammetry (CV) measurements were performed in a three-electrode system: glassy carbon (0.07 cm^2) as the working electrode (WE), graphite as the counter electrode (CE), and Ag/AgCl (0.1 M LiTFSI in MeCN) as the pseudoreference electrode (RE) with ferrocene/ferrocenium (Fc/Fc^+) in the electrolyte as a reference. Acetonitrile (80%), chlorobenzene (20%), and LiTFSI (1.0 M) served as supporting electrolytes. (Each germanium compound (0.5 mM) was dissolved in each solution.) This solvent mixture was due to the small solubility of the compounds in MeCN.

Experimental Determination of HOMO and LUMO. The highest occupied molecular orbital (HOMO) energy levels were derived from the ground-state oxidation potential obtained from the onset values of the first oxidation potential of the cyclic voltammetry measurements of compounds in solutions described above. In contrast, the lowest unoccupied molecular orbital (LUMO) energy levels were estimated on adding the optical band gap (E_g) (obtained from the recording of the UV−visible solid-state spectra) to the HOMO energy levels. Potentials were converted to the standard hydrogen electrode (SHE) with correction +0.624 V[S1] and then to the vacuum scale with correction 4.4 eV.

Calculations with Density Functional Theory (DFT). Molecular and periodic calculations for compounds **1**−**4** were undertaken with the TURBOMOLE quantum chemical package. Molecular calculations were performed at the BP86/def2-TZVP and TD-BP86/def2-TZVP levels of theory for ground and electronically excited states, respectively. Initial structures for the optimizations of molecular geometries of **1** and **4** were based on their corresponding X-ray crystal structures; for compounds **2** and **3**, the initial structure was based on that of **4**. All geometries were tightly converged. All minimum structures were corroborated on computing analytical second derivatives of the energy with respect to the nuclear coordinates. Calculations on the periodic systems were performed with the BP86 pure functional, in conjunction with all-electron basis set def2-TZVP for all atoms except hydrogen, for which def2-SV(P) was used. Making use of the same strategy, which was taken for the molecular calculations, the structures of unit cells for the geometry optimizations of **1** and **4** were based on their corresponding X-ray crystal structures. In contrast, for compounds **2** and **3**, the initial structures were based on that of **4**. All geometry optimizations and band structure calculations were undertaken with a $6 \times 6 \times 6$ k-point mesh grid size. The density of states and the respective atomic orbital contributions were obtained with a convolution of Gaussian functions on the discrete energy levels. Both molecular and periodic calculations were conducted with the resolution of identity approximation (RI approximation) for the computation of the four-center integrals. At the same time, the calculation for periodic systems also included the continuous fast multipole method (CFMM) for the electronic Coulomb term.

Space−Charge-Limited Current (SCLC). The method of space−charge-limited current (SCLC) was applied to hole-only devices (FTO/Ge-compound/Au) using current−voltage (J−V) curves. Vertical hole mobility values were fitted using the Mott−Gurney law and calculated according to $J = 9/8e_re_0\mu V^2L^{-3}$; J, e_r, e_0, μ, V, and L denote the current, relative permittivity (e_r = 3 was used here), vacuum permittivity, hole mobility, applied voltage, and film thickness, respectively.

Images from a Scanning Electron Microscope (SEM). These SEM images were collected (high-resolution Gemini SEM 300) with a field-emission gun.

Current Density−Voltage (J−V) Curves. Current density−voltage (J−V) curves and the time-dependent efficiency of power conversion (PCE) of the devices were measured with a xenon lamp (450 W, Oriel). To calibrate the light intensity, we used a Si photodiode equipped with an IR cutoff filter (KG3, Schott) during each measurement as well as 1.5 AM conditions. J−V parameters of the devices were obtained on applying an external voltage bias while measuring the current response with a digital source meter (Keithley 2400). A black metal mask (area 0.16 cm^2) was used during the measurements to avoid overestimation from scattered light.

https://dx.doi.org/10.1021/acs.inorgchem.0c02120
Inorg. Chem. 2020, 59, 15154−15166

X-ray Diffraction Analysis. Monocrystals of compound **4** were selected from the mother solution and covered with perfluorinated polyether oil on a microscope slide, which was cooled with flowing dinitrogen gas. The data of compound **4** were collected at 100 K in a dual-source configuration (Mo and Cu, Bruker D8 Venture), three-circle diffractometer equipped with a CCD detector (Photon CMOS APEX III) and a Mo Kα (λ = 0.71073 Å) microfocus source (INCOATEC)[62] with Quazar mirror optics (INCOATEC Q). All data were integrated with SAINT;[63] semiempirical absorption corrections were applied with SADABS.[64] The structure was solved with direct methods (SHELXS-97)[65] and refined against all data with full-matrix least-squares methods on F^2 (SHELXL2013)[66,67] inside the SHELXLE GUI.[68] All non-hydrogen atoms were refined with anisotropic displacement parameters. All hydrogen atoms were refined on calculated positions using a riding model. Their U_{iso} values were constrained to 1.5U_{eq} of their pivot atoms for terminal tetrahedrally coordinated carbon atoms and to 1.2U_{eq} for all other carbon atoms. All bond lengths and angles of **4** are shown in the Supporting Information (SI).

■ ASSOCIATED CONTENT

Supporting Information

The Supporting Information is available free of charge at https://pubs.acs.org/doi/10.1021/acs.inorgchem.0c02120.

^{1}H, ^{13}C, and ^{77}Se NMR spectra, cost-analysis estimation, and *E* factor; table of crystal data, structure refinement details, and selected bond lengths and angles for compound **4**; quantum chemical calculations and DFT results, additional DSC figures, UV−visible spectra, and CV; hysteresis; and statistics and optimization plots (PDF)

Accession Codes

CCDC 1867214 contains the supplementary crystallographic data for this paper. These data can be obtained free of charge via www.ccdc.cam.ac.uk/data_request/cif, or by emailing data_request@ccdc.cam.ac.uk, or by contacting The Cambridge Crystallographic Data Centre, 12 Union Road, Cambridge CB2 1EZ, UK; fax: +44 1223 336033.

■ AUTHOR INFORMATION

Corresponding Authors

Cristopher Camacho − *Escuela de Química, Universidad de Costa Rica, 11501-2060 San José, Costa Rica;* orcid.org/0000-0002-5667-9505; Email: cristopher.camacho@ucr.ac.cr

Anders Hagfeldt − *Laboratory of Photomolecular Science, Institute of Chemistry Sciences and Engineering, School of Basic Science, École Polytechnique Fédérale de Lausanne, CH-1015 Lausanne, Switzerland;* orcid.org/0000-0001-6725-8856; Email: anders.hagfeldt@epfl.ch

Leslie W. Pineda − *Centro de Investigación en Electroquímica y Energía Química (CELEQ) and Escuela de Química, Universidad de Costa Rica, 11501-2060 San José, Costa Rica;* orcid.org/0000-0003-3778-6185; Email: leslie.pineda@ucr.ac.cr

Authors

Tatiana Soto-Montero − *Centro de Investigación en Electroquímica y Energía Química (CELEQ), Universidad de Costa Rica, 11501-2060 San José, Costa Rica*

Natalie Flores-Díaz − *Laboratory of Photomolecular Science, Institute of Chemistry Sciences and Engineering, School of Basic Science, École Polytechnique Fédérale de Lausanne, CH-1015 Lausanne, Switzerland*

Desiré Molina − *Área de Química Orgánica, Instituto de Bioingeniería, Universidad Miguel Hernández, 03202 Elche, Spain*

Andrea Soto-Navarro − *Centro de Investigación en Electroquímica y Energía Química (CELEQ), Universidad de Costa Rica, 11501-2060 San José, Costa Rica*

Andrés Lizano-Villalobos − *Escuela de Química, Universidad de Costa Rica, 11501-2060 San José, Costa Rica*

Complete contact information is available at: https://pubs.acs.org/10.1021/acs.inorgchem.0c02120

Notes

The authors declare no competing financial interest.

■ ACKNOWLEDGMENTS

This work is dedicated to Professor Herbert W. Roesky on the occasion of his 85th birthday. Centro de Electroquímica y Energía Química (CELEQ, UCR) and Escuela de Química (D8 Venture SC XRD, UCR) supported this work. T.S.-M. is grateful for an Orlando Bravo scholarship (CELEQ) for support and Sistema de Estudios de Posgrado (SEP, UCR) and Vicerrectoría de Investigación (VI, UCR, grant 804-B7-271) for a research stay at EPFL. C.C. acknowledges financial support from VI, UCR (grant 115-B9-461) and thanks Roberto A. González−León for technical assistance. D.M. thanks the European Union through the "Programa Operativo del Fondo Social Europeo (FSE) de la Comunitat Valenciana 2014-2020" for grant APOSTD/2017/026. Dr. Aurélien Bornet from the NMR team of ISIC, EPFL, is greatly acknowledged for his assistance with the ^{77}Se NMR experiment and the NMR unit of Escuela de Química at UCR.

■ ABBREVIATIONS

HTM, hole-transport material; VB, valence band; CB, conduction band; UV, ultraviolet; DFT, density functional theory; IR, infrared; NMR, nuclear magnetic resonance

■ REFERENCES

(1) Kojima, A.; Teshima, K.; Shirai, Y.; Miyasaka, T. Organometal Halide Perovskites as Visible-Light Sensitizers for Photovoltaic Cells. *J. Am. Chem. Soc.* **2009**, *131* (17), 6050−6051.

(2) National Renewable Energy Laboratory (NREL). Best Research-Cell Efficiency Chart 2020.

(3) Dunlap-Shohl, W. A.; Zhou, Y.; Padture, N. P.; Mitzi, D. B. Synthetic Approaches for Halide Perovskite Thin Films. *Chem. Rev.* **2019**, *119* (5), 3193−3295.

(4) Savenije, T.; Ponseca, C. J.; Kunneman, L.; Abdellah, M.; Zheng, K.; Tian, Y.; Zhu, Q.; Canton, S.; Scheblykin, I.; Pullerits, T.; Yartsev, A.; Sundström, V. Thermally Activated Exciton Dissociation and Recombination Control the Carrier Dynamics in Organometal Halide Perovskite. *J. Phys. Chem. Lett.* **2014**, *5* (13), 2189−2194.

(5) Stranks, S.; Eperon, G.; Grancini, G.; Menelaou, C.; Alcocer, M.; Leijtens, T.; Herz, L.; Petrozza, A.; Snaith, H. J. Electron-Hole Diffusion Lengths Exceeding 1 Micrometer in an Organometal Trihalide Perovskite Absorber. *Science* **2013**, *342* (6156), 341−344.

(6) Noh, J. H.; Im, S. H.; Heo, J. H.; Mandal, T. N.; Seok, S. Il. Chemical Management for Colorful, Efficient, and Stable Inorganic-Organic Hybrid Nanostructured Solar Cells. *Nano Lett.* **2013**, *13* (4), 1764−1769.

(7) Reyna, Y.; Salado, M.; Kazim, S.; Pérez-Tomas, A.; Ahmad, S.; Lira-Cantu, M. Performance and Stability of Mixed FAPbI$_{3(0.85)}$MAPbBr$_{3(0.15)}$ Halide Perovskite Solar Cells under Outdoor Conditions and the Effect of Low Light Irradiation. *Nano Energy* **2016**, *30*, 570−579.

(8) Park, N.-G.; Grätzel, M.; Miyasaka, T.; Zhu, K.; Emery, K. Towards Stable and Commercially Available Perovskite Solar Cells. *Nature Energy* **2016**, *1* (11), 16152.
(9) Lee, J. W.; Kim, H. S.; Park, N. G. Lewis Acid-Base Adduct Approach for High Efficiency Perovskite Solar Cells. *Acc. Chem. Res.* **2016**, *49* (2), 311−319.
(10) Ahn, N.; Son, D. Y.; Jang, I. H.; Kang, S. M.; Choi, M.; Park, N. G. Highly Reproducible Perovskite Solar Cells with Average Efficiency of 18.3% and Best Efficiency of 19.7% Fabricated via Lewis Base Adduct of Lead(II) Iodide. *J. Am. Chem. Soc.* **2015**, *137* (27), 8696−8699.
(11) Burschka, J.; Pellet, N.; Moon, S.-J.; Humphry-Baker, R.; Gao, P.; Nazeeruddin, M. K.; Grätzel, M. Sequential Deposition as a Route to High-Performance Perovskite-Sensitized Solar Cells. *Nature* **2013**, *499* (7458), 316−319.
(12) Jeon, N. J.; Noh, J. H.; Yang, W. S.; Kim, Y. C.; Ryu, S.; Seo, J.; Seok, S. Il. Compositional Engineering of Perovskite Materials for High-Performance Solar Cells. *Nature* **2015**, *517* (7535), 476−480.
(13) Pellet, N.; Gao, P.; Gregori, G.; Yang, T. Y.; Nazeeruddin, M. K.; Maier, J.; Grätzel, M. Mixed-Organic-Cation Perovskite Photovoltaics for Enhanced Solar-Light Harvesting. *Angew. Chem., Int. Ed.* **2014**, *53* (12), 3151−3157.
(14) Bi, D.; Luo, J.; Zhang, F.; Magrez, A.; Athanasopoulou, E. N.; Hagfeldt, A.; Grätzel, M. Morphology Engineering: A Route to Highly Reproducible and High Efficiency Perovskite Solar Cells. *ChemSusChem* **2017**, *10* (7), 1624−1630.
(15) Ravishankar, S.; Gharibzadeh, S.; Roldan-Carmona, C.; Grancini, G.; Lee, Y.; Ralaiarisoa, M.; Asiri, A. M.; Koch, N.; Bisquert, J.; Nazeeruddin, M. K. Influence of Charge Transport Layers on Open-Circuit Voltage and Hysteresis in Perovskite Solar Cells Influence of Charge Transport Layers on Open-Circuit Voltage and Hysteresis in Perovskite Solar Cells. *Joule* **2018**, *2*, 788.
(16) Yang, X.; Wang, H.; Cai, B.; Yu, Z.; Sun, L. Progress in Hole-Transporting Materials for Perovskite Solar Cells. *J. Energy Chem.* **2018**, *27*, 650.
(17) (a) Rakstys, K.; Igci, C.; Nazeeruddin, M. K. Efficiency *vs.* stability: dopant-free hole transporting materials towards stabilized perovskite solar cells. *Chem. Sci.* **2019**, *10*, 6748−6769. (b) Molina, D.; Ruiz-Preciado, M. A.; Sadegh, F.; Álvaro-Martins, M. J.; Grätzel, M.; Hagfeldt, A.; Sastre-Santos, Á. p-Phenylene-bridged zinc phthalocyanine-dimer as hole-transporting material in perovskite solar cells. *J. Porphyrins Phthalocyanines* **2019**, *23*, 546−553. (c) Jeon, N. J.; Lee, H. G.; Kim, Y. C.; Seo, J.; Noh, J. H.; Lee, J.; Seok, S. Il. O-Methoxy Substituents in Spiro-OMeTAD for Efficient Inorganic−Organic Hybrid Perovskite Solar Cells. *J. Am. Chem. Soc.* **2014**, *136* (22), 7837−7840.
(18) Xi, H.; Tang, S.; Ma, X.; Chang, J.; Chen, D.; Lin, Z.; Zhong, P.; Wang, H.; Zhang, C. Performance Enhancement of Planar Heterojunction Perovskite Solar Cells through Tuning the Doping Properties of Hole-Transporting Materials. *ACS Omega* **2017**, *2* (1), 326−336.
(19) Seo, J.-Y.; Kim, H.-S.; Akin, S.; Stojanovic, M.; Simon, E.; Fleischer, M.; Hagfeldt, A.; Zakeeruddin, S. M.; Grätzel, M. Novel p-Dopant toward Highly Efficient and Stable Perovskite Solar Cells. *Energy Environ. Sci.* **2018**, *11*, 2985−2992.
(20) Zhao, X.; Kim, H. S.; Seo, J. Y.; Park, N. G. Effect of Selective Contacts on the Thermal Stability of Perovskite Solar Cells. *ACS Appl. Mater. Interfaces* **2017**, *9* (8), 7148−7153.
(21) Kim, H.-S.; Seo, J.-Y.; Park, N.-G. Impact of Selective Contacts on Long-Term Stability of $CH_3NH_3PbI_3$ Perovskite Solar Cells. *J. Phys. Chem. C* **2016**, *120* (49), 27840−27848.
(22) (a) Madhavan, V. E.; Zimmermann, I.; Baloch, A. A. B.; Manekkathodi, A.; Belaidi, A.; Tabet, N.; Nazeeruddin, M. K. CuSCN as Hole Transport Material with 3D/2D Perovskite Solar Cells. *ACS Appl. Energy Mater.* **2020**, *3*, 114−121. (b) Calió, L.; Kazim, S.; Grätzel, M.; Ahmad, S. Hole-Transport Materials for Perovskite Solar Cells. *Angew. Chem., Int. Ed.* **2016**, *55* (47), 14522−14545.
(23) Jiang, K.; Wu, F.; Zhang, G.; Zhu, L.; Yan, H. Efficient Perovskite Solar Cells Based on Dopant-Free Spiro-OMeTAD Processed With Halogen-Free Green Solvent. *Sol. RRL* **2019**, *3*, 1900061.
(24) Cao, Y.; Li, Y.; Morrissey, T.; Lam, B.; Patrick, B. O.; Dvorak, D. J.; Xia, Z.; Kelly, T. L.; Berlinguette, C. P. Dopant-free molecular hole transport material that mediates a 20% power conversion efficiency in a perovskite solar cell. *Energy Environ. Sci.* **2019**, *12*, 3502−3507.
(25) Molina, D.; Ruiz-Preciado, M. A.; Carlsen, B.; Eickemeyer, F. T.; Yang, B.; Flores-Díaz, N.; Álvaro-Martins, M. J.; Nonomura, K.; Hagfeldt, A.; Sastre-Santos, Á. Zinc Phthalocyanine Conjugated Dimers as Efficient Dopant-Free Hole Transporting Materials in Perovskite Solar Cells. *ChemPhotoChem.* **2020**, *4*, 307−314.
(26) Chou, H.-H.; Chiang, Y.-H.; Chen, Y.-H.; Guo, C.-J.; Zuo, H.-Y.; Cheng, W.-T.; Lin, P.-Y.; Chiu, Y.-Y.; Chen, P.; Yeh, C.-Y. Porphyrin-Based Simple and Practical Dopant-Free Hole-Transporting Materials for Efficient Perovskite Solar Cells Using TiO_2 Semiconductors. *Sol. RRL* **2020**, *4*, 2000119.
(27) Yu, Z.; Sun, L. Recent Progress on Hole-Transporting Materials for Emerging Organometal Halide Perovskite Solar Cells. *Adv. Energy Mater.* **2015**, *5*, 1500213.
(28) (a) Boyle, T. J.; Tribby, L. J.; Ottley, L. A. M.; Han, S. M. Synthesis and Characterization of Germanium Coordination Compounds for Production of Germanium Nanomaterials. *Eur. J. Inorg. Chem.* **2009**, *36*, 5550−5560. (b) Mitzi, D. B. Synthesis, Structure, and Thermal Properties of Soluble Hydrazinium Germanium(IV) and Tin(IV) Selenide Salts. *Inorg. Chem.* **2005**, *44*, 3755−3761. (c) Mitzi, D. B. Synthesis, Crystal Structure, and Optical and Thermal Properties of $(C_4H_9NH_3)_2MI_4$ (M = Ge, Sn, Pb). *Chem. Mater.* **1996**, *8*, 791−800.
(29) Chou, H.; Chiang, Y.; Li, M.; Shen, P.; Wei, H.; Mai, C.; Chen, P.; Yeh, C. Zinc Porphyrin−Ethynylaniline Conjugates as Novel Hole-Transporting Materials for Perovskite Solar Cells with Power Conversion Efficiency of 16.6%. *ACS Energy Lett.* **2016**, *1*, 956−962.
(30) Chiang, Y.; Chou, H.; Cheng, W.; Li, Y.; Yeh, C.; Chen, P. Porphyrin Dimers as Hole-Transporting Layers for High-Efficiency and Stable Perovskite Solar Cells. *ACS Energy Lett.* **2018**, *3*, 1620−1626.
(31) Li, B.; Zheng, C.; Liu, H.; Zhu, J.; Zhang, H.; Gao, D.; Huang, W. Large Planar π-Conjugated Porphyrin for Interfacial Engineering in p-i-n Perovskite Solar Cells. *ACS Appl. Mater. Interfaces* **2016**, *8*, 27438−27443.
(32) Gao, K.; Xiao, L.; Kan, Y.; Yang, B.; Peng, J.; Cao, Y.; Liu, F.; Russell, T.; Peng, X. Solution-Processed Bulk Heterojunction Solar Cells Based on Porphyrin Small Molecules with Very Low Energy Losses Comparable to Perovskite Solar Cells and High Quantum Efficiencies. *J. Mater. Chem. C* **2016**, *4* (17), 3843−3850.
(33) Bourget-Merle, L.; Lappert, M. F.; Severn, J. R. The Chemistry of β-Diketiminatometal Complexes. *Chem. Rev.* **2002**, *102*, 3031−3066.
(34) Pineda, L. W.; Jancik, V.; Roesky, H. W.; Herbst-Irmer, R. OH Functionality of Germanium(II) Compounds for the Formation of Heterobimetallic Oxides. *Inorg. Chem.* **2005**, *44*, 3537−3540.
(35) Pineda, L. W.; Jancik, V.; Starke, K.; Oswald, R. B.; Roesky, H. W. Stable Monomeric Germanium(II) and Tin(II) Compounds with Terminal Hydrides. *Angew. Chem., Int. Ed.* **2006**, *45* (16), 2602−2605.
(36) Pineda, L. W.; Jancik, V.; Oswald, R. B.; Roesky, H. W. Preparation of LGe(Se)OH: A Germanium Analogue of a Selenocarboxylic Acid (L = $HC[(CMe)(NAr)]_2$, Ar = 2,6-iPr$_2$C$_6$H$_3$). *Organometallics* **2006**, *25* (9), 2384−2387.
(37) Ballestero-Martínez, E.; Klosin, J.; Fahlman, B. D.; Pineda, L. W. Monomeric Germanium(II) Amides Bearing β-Diketiminato Ligands: Synthesis, Structural Characterization, and Thermal Properties. *Eur. J. Inorg. Chem.* **2014**, *2014* (30), 5233−5239.
(38) Hohloch, S.; Kriegel, B. M.; Bergman, R. G.; Arnold, J. Group 5 Chemistry Supported by β-Diketiminate Ligands. *Dalton Trans.* **2016**, *45* (40), 15725−15745.
(39) Sheldon, R. A. E Factors, Green Chemistry and Catalysis: An Odyssey. *Chem. Commun.* **2008**, 3352−3365.

https://dx.doi.org/10.1021/acs.inorgchem.0c02120
Inorg. Chem. 2020, 59, 15154−15166

(40) Petrus, M. L.; Music, A.; Closs, A. C.; Bijleveld, J.; Sirtl, M.; Hu, Y.; Dingemans, T. J.; Bein, T.; Docampo, P. Design Rules for the Preparation of Low-Cost Hole Transporting Materials for Perovskite Solar Cells with Moisture Barrier Properties. *J. Mater. Chem. A* **2017**, *5*, 25200−25210.
(41) Ding, Y.; Roesky, H. W.; Noltemeyer, M.; Schmidt, H.-G. Synthesis and Structures of Monomeric Divalent Germanium and Tin Compounds Containing a Bulky Diketiminato Ligand. *Organometallics* **2001**, *20*, 1190−1194.
(42) Ding, Y.; Ma, Q.; Roesky, H. W.; Usón, I.; Noltemeyer, M.; Schmidt, H. Syntheses, Structures and Properties of [{HC(CMeNAr)$_2$}Ge(E)X] (Ar = 2,6-*i*Pr$_2$C$_6$H$_3$; E = S, Se; X = F, Cl. *Dalton Trans.* **2003**, 1094−1098.
(43) Petrus, M. L.; Bein, T.; Dingemans, T. J.; Docampo, P. A Low Cost Azomethine-Based Hole Transporting Material for Perovskite Photovoltaics. *J. Mater. Chem. A* **2015**, *3* (23), 12159−12162.
(44) Sharma, M. K.; Sinhababu, S.; Yadav, D.; Mukherjee, G.; Rajaraman, G.; Nagendran, S. Pseudohalogenogermylenes versus Halogenogermylenes: Difference in Their Complexation Behavior towards Group 6 Metal Carbonyls. *Chem. - Asian J.* **2018**, *13* (10), 1357−1365.
(45) Rakstys, K.; Abate, A.; Dar, M. I.; Gao, P.; Jankauskas, V.; Jacopin, G.; Kamarauskas, E.; Kazim, S.; Ahmad, S.; Grätzel, M.; Nazeeruddin, M. K. Triazatruxene-Based Hole Transporting Materials for Highly Efficient Perovskite Solar Cells. *J. Am. Chem. Soc.* **2015**, *137*, 16172−16178.
(46) Gehlhaar, R.; Merckx, T.; Qiu, W.; Aernouts, T. Outdoor Measurement and Modeling of Perovskite Module Temperatures. *Global Challenges* **2018**, *2* (7), 1800008.
(47) Ma, S.; Zhang, H.; Zhao, N.; Cheng, Y.; Wang, M.; Shen, Y.; Tu, G. Spiro-Thiophene Derivatives as Hole-Transport Materials for Perovskite Solar Cells. *J. Mater. Chem. A* **2015**, *3* (23), 12139−12144.
(48) Daskeviciu te, S.; Sakai, N.; Franckevicius, M.; Daskeviciene, M.; Magomedov, A.; Jankauskas, V.; Snaith, H. J.; Getautis, V. Nonspiro, Fluorene-Based, Amorphous Hole Transporting Materials for Efficient and Stable Perovskite Solar Cells. *Adv. Sci.* **2018**, *5* (4), 1700811.
(49) Malinauskas, T.; Tomkute-Luksiene, D.; Sens, R.; Daskeviciene, M.; Send, R.; Wonneberger, H.; Jankauskas, V.; Bruder, I.; Getautis, V. Enhancing Thermal Stability and Lifetime of Solid-State Dye-Sensitized Solar Cells via Molecular Engineering of the Hole-Transporting Material Spiro-OMeTAD. *ACS Appl. Mater. Interfaces* **2015**, *7* (21), 11107−11116.
(50) López, R.; Gómez, R. Band-Gap Energy Estimation from Diffuse Reflectance Measurements on Sol-Gel and Commercial TiO_2: A Comparative Study. *J. Sol-Gel Sci. Technol.* **2012**, *61* (1), 1−7.
(51) Pavlishchuk, V.; Addison, A. W. Conversion Constants for Redox Potentials Measured versus Different Reference Electrodes in Acetonitrile Solutions at 25 °C. *Inorg. Chim. Acta* **2000**, *298* (1), 97−102.
(52) Correa Baena, J. P.; Steier, L.; Tress, W.; Saliba, M.; Neutzner, S.; Matsui, T.; Giordano, F.; Jacobsson, T. J.; Srimath Kandada, A. R.; Zakeeruddin, S. M.; Petrozza, A.; Abate, A.; Nazeeruddin, M. K.; Grätzel, M.; Hagfeldt, A. Highly Efficient Planar Perovskite Solar Cells through Band Alignment Engineering. *Energy Environ. Sci.* **2015**, *8* (10), 2928−2934.
(53) Snaith, H. J.; Grätzel, M. Enhanced Charge Mobility in a Molecular Hole Transporter via Addition of Redox Inactive Ionic Dopant: Implication to Dye-Sensitized Solar Cells. *Appl. Phys. Lett.* **2006**, *89*, 262114.
(54) Moiz, S. A.; Khan, I. A.; Younis, W. A.; Karimov, K. S. Space Charge−Limited Current Model for Polymers. *Conducting Polymers; INTECH*; InTech, 2016; pp 91−105.
(55) Saliba, M.; Matsui, T.; Seo, J.-Y.; Domanski, K.; Correa-Baena, J.-P.; Nazeeruddin, M. K.; Zakeeruddin, S. M.; Tress, W.; Abate, A.; Hagfeldt, A.; Grätzel, M. Cesium-Containing Triple Cation Perovskite Solar Cells: Improved Stability, Reproducibility and High Efficiency. *Energy Environ. Sci.* **2016**, *9* (6), 1989−1997.
(56) (a) Park, B.-W.; Jain, S. M.; Zhang, X.; Hagfeldt, A.; Boschloo, G.; Edvinsson, T. Resonance Raman and Excitation Energy Dependent Charge Transfer Mechanism in Halide-Substituted Hybrid Perovskite Solar Cells. *ACS Nano* **2015**, *9*, 2088−2101. (b) Shen, Q.; Ogomi, Y.; Chang, J.; Tsukamoto, S.; Kukihara, K.; Oshima, T.; Osada, N.; Yoshino, K.; Katayama, K.; Toyoda, T.; Hayase, S. Charge transfer and recombination at the metal oxide/$CH_3NH_3PbCl_2$/*spiro*-OMeTAD interfaces: uncovering the detailed mechanism behind high efficiency solar cells. *Phys. Chem. Chem. Phys.* **2014**, *16*, 19984−19992.
(57) Wang, Z.; Baranwal, A. K.; Kamarudin, M. A.; Chi Huey, N.; Pandey, M.; Ma, T.; Hayase, S. Xanthate-induced sulfur doped all-inorganic perovskite with superior phase stability and enhanced performanced. *Nano Energy* **2019**, *59*, 258−267.
(58) Wang, Z.; Kamarudin, M. A.; Chi Huey, N.; Yang, F.; Pandey, M.; Kapil, G.; Ma, T.; Hayase, S. Interfacial Sulfur Functionalization Anchoring SnO_2 and $CH_3NH_3PbI_3$ for Enhanced Stability and Trap Passivation in Perovskite Solar Cells. *ChemSusChem* **2018**, *11*, 3941−3948.
(59) Ebels, J.; Spirk, S.; Pietsching, R. *10th International Electronic Conference on Synthetic Organic Chemistry (ECSOC-10)*; 2006; pp 1−4.
(60) Harris, R. K.; Becker, E. D.; Cabral de Menezes, S. M.; Granger, P.; Hoffman, R. E.; Zilm, K. W. Further Conventions for NMR Shielding and Chemical Shifts. *Pure Appl. Chem.* **2008**, *80* (1), 59−84.
(61) Stender, M.; Wright, R. J.; Eichler, B. E.; Prust, J.; Olmstead, M. M.; Roesky, H. W.; Power, P. P. The synthesis and structure of lithium derivatives of the sterically encumbered *β*-diketiminate ligand [{(2,6-Pr$^i_2$H$_3$C$_6$)N(CH$_3$)C}CH]$^-$, and a modified synthesis of the aminoimine precursor. *J. Chem. Soc. Dalt. Trans.* **2001**, 3465−3469.
(62) Schulz, T.; Meindl, K.; Leusser, D.; Stern, D.; Graf, J.; Michaelsen, C.; Ruf, M.; Sheldrick, G. M.; Stalke, D. A Comparison of a Microfocus X-Ray Source and a Conventional Sealed Tube for Crystal Structure Determination. *J. Appl. Crystallogr.* **2009**, *42* (5), 885−891.
(63) *SAINT*; Bruker AXS Inc.: Madison, WI (EEUU), 2000.
(64) Sheldrick, G. M. *SADABS*; Universität Göttingen: Germany, 2000.
(65) Sheldrick, G. M. Phase Annealing in SHELX-90: Direct Methods for Larger Structures. *Acta Crystallogr., Sect. A: Found. Crystallogr.* **1990**, *46* (6), 467−473.
(66) Sheldrick, G. M. A Short History of SHELX. *Acta Crystallogr., Sect. A: Found. Crystallogr.* **2008**, *64* (1), 112−122.
(67) Müller, P.; Herbst-Imer, R.; Spek, A. L.; Schneider, T. R.; Sawaya, M. R. *Crystal Structure Refinement: A Crystallographer's Guide to SHELXL, IUCr Texts on Crystallography*; Müller, P., Ed.; Oxford University Press: Oxford, U.K., 2006.
(68) Hübschle, C. B.; Sheldrick, G. M.; Dittrich, B. ShelXle: A Qt Graphical User Interface for SHELXL. *J. Appl. Crystallogr.* **2011**, *44* (6), 1281−1284.

https://dx.doi.org/10.1021/acs.inorgchem.0c02120
Inorg. Chem. 2020, 59, 15154−15166